Modelling the fluid-structure interactions of a capsule using a nonlinear thin shell model: effect of wall thickness

Claire Dupont, Marina Vidrascu, Patrick Le Tallec, Dominique Barthès-Biesel, Anne-Virginie Salsac

Modelling the fluid–structure interactions of a capsule using a nonlinear thin shell model: effect of wall thickness

C. Dupont[1], M. Vidrascu[2], P. Le Tallec[3], D. Barthès-Biesel[1], A.-V. Salsac[1*]

[1] *Biomechanics and Bioengineering Laboratory (UMR 7338), Université de Technologie de Compiègne - CNRS, 60203 Compiègne, France*

[2] *Commedia Team, Inria Paris - Laboratoire J.L. Lions (Sorbonne Université CNRS), 75012 Paris, France*

[3] *Laboratoire de Mécanique des Solides, Ecole Polytechnique, CNRS, Institut Polytechnique de Paris, 91128 Palaiseau, France*

Abstract

We address the question of the modelling of the fluid-structure interactions for a microcapsule enclosed by a finite-thickness wall, and of the prediction of the buckling behaviour when it is subjected to large displacements and deformations. Specifically, we model the strong coupling between the solid (the wall dynamics) and fluid (the flow inside and outside the capsule) mechanics, for a wall material that can be strain-hardening or softening, while accounting for the bending resistance due to thickness. The fluid flow is assumed to be inertialess on the capsule scale, which allows the use of the boundary integral formulation for the fluid velocity. We discuss the different simplifications that are made when designing a fluid–shell interaction model for large deformations, and present a shear-membrane-bending (SMB) shell model that allows for a nonlinear wall stretching law. The performance of the model, as compared to a simple membrane model where bending resistance is neglected, is illustrated on a generic example: we consider an initially ellipsoidal capsule, freely suspended in a plane hyperbolic flow, that is subjected to such stringent deformation, that its short axis becomes the long one. We show that the simple membrane model predicts reasonably well the overall shape of the capsule, but cannot capture the detailed post buckling behaviour, for which a robust shell model is necessary. The SMB shell model complies with dominant membrane effects, remains stable even under large deformation and avoids numerical locking. It allows predicting post-buckling behaviour, which depends on the material constitutive law.

Keywords: fluid-structure interactions, numerical simulations, microcapsules, shell

*Corresponding author. E-mail: anne-virginie.salsac@utc.fr

1. Introduction

Capsules consisting of a liquid drop enclosed by a thin deformable wall are ubiquitous particles in nature (cells) or in industry. Usually the membrane is as thin as possible, to maximize the payload (internal contents) and facilitate trans-wall exchanges, while guaranteeing the particle integrity under stress. Consequently, when suspended in another liquid undergoing flow, the capsules may deform significantly (this would not be the case for a thick-walled capsule, which can then be treated as a rigid particle). For example an initially spherical capsule will become roughly ellipsoidal in simple shear flow [1, 2, 3] or will take a slug shape in tube flow as illustrated in Figure 1 [4, 5, 6]. During the deformation process and depending on the flow strength, some parts of the capsule membrane may buckle or exhibit significant curvature changes, e.g. when they take a parachute shape (Figure 1).

Modelling those phenomena represents a challenging fluid–structure interaction (FSI) problem: (i) the capsule wall undergoes large deformations and large displacement, which must be taken into account in the solid mechanics part of the problem; (ii) inertia effects are small, so that the velocity and pressure fields depend on the deformed shape of the capsule; (iii) the capsule is a closed surface that is typically freely suspended in another liquid. Consequently, the classical implicit FSI numerical scheme, where forces are imposed and displacements determined from the solid problem is cumbersome and not adapted to the problem at stake. Another option is to follow the position of the nodes of the capsule (Lagrangian tracking) and to solve for the loads acting on the capsule. This numerical scheme has the advantage of being stable at low inertia [7]. Whatever fluid solver is used, the overall resolution scheme is then explicit: knowing the load exerted by the solid, the fluid solver computes the velocity field, from which the displacement of the membrane points is computed; the solid solver then recomputes the load on the fluid and the process is repeated until a steady state is reached. Since the solid solver operates in opposite fashion to the traditional finite element schemes, commercial or free-ware shell codes cannot be used directly and have to be modified (when possible).

Many models treat the capsule wall as an infinitely thin membrane (i.e. an elastic surface) with negligible bending resistance (see the review article by [8]). Although such models can identify the regions where the wall is undergoing compression, they cannot model correctly the post-buckling

behaviour. When bending effects are included, a Eulerian thin shell model (Helfrich model) is often used where the bending resistance is assumed to be proportional to the local change of curvature [9, 10, 11, 12, 13, 14]. However, very large values of the bending modulus must be used to find any influence on the deformation of a spherical capsule in simple shear flow. It follows that such models are appropriate to model capsule walls with strong anisotropy such as lipid bilayers.

The Helfrich model is not appropriate to model artificial capsules with an isotropic homogeneous membrane obtained through interfacial polymerization or coating [15, 16, 4]. For those capsules, the resistance to bending is specifically linked to the thickness of the wall. Of course, when the wall is thin, the bending resistance is low. Nevertheless, under certain flow conditions bending effects become important: this happens when the membrane buckles and makes folds (observed in simple shear, plane hyperbolic or pore flows) as shown in Figure 1 or when the membrane locally changes its curvature (parachute shape). Since capsules can deform significantly, it is important to design a mechanical model that can account for the nonlinear elastic behaviour of the wall material and include bending resistance due to a small but finite thickness.

A first thin shell model was developed by Le & Tan [17], but it was based on a Kirchhoff-Love assumption, which neglects transverse shear. Dupont et al. [18] considered instead a thin shell model based on Reissner-Mindlin assumption to model a capsule subjected to an inertialess simple shear flow. They modified the shell finite element Shelddon library, designed by Inria[1] to compute the load from the displacement, while accounting for large mid-surface deformation. The velocity field was then obtained from a boundary integral computed on the capsule mid-surface. They showed that it was possible to compute the post-buckling behaviour of an initially spherical capsule subjected to a simple shear or a plane hyperbolic flow and analyzed the wrinkles that form on the membrane as a function of flow strength and membrane bending resistance [18, 19]. However, their model was limited to the generalized Hooke's material law, which is strain-hardening, and the model cannot be extended to any other law. This is a limitation, since it was shown that, for some capsules, the membrane material was strain-softening [4, 6, 20].

Different options exist to account for the non-linear mechanical behaviour of the material: (i)

[1]The Shelddon library is registered at the *Agence pour la Protection des Programmes* (ref IDDN.FR.001.030018.000.S.P.2010.000.20600). The base of the program is open source and available online: www-rocq.inria.fr/modulef.

Using 3D finite elements (i.e. without the shell hypothesis) is one option, but the model resolution is often unstable. (ii) Using thick shells that account for the non-linearity behaviour layer by layers is another one, but it requires very long computation times is not necessarily relevant for capsules, for which the main force contribution within the wall remains the tangential elastic traction force (the membrane force tends to remain dominant over the bending force for a very large range of parameters). The option that we propose is based on another modelling approach: a shear-membrane-bending model, which decouples membrane and bending forces by simplifying the curvature terms. It is thus adequate for small to moderate capsule thicknesses. The approach provides a fully 3D model, with the shell kinematics fully described across the thickness. The advantage of such model is that the elastic law can be easily modified and that one can use all the material laws of membrane models.

We model the post-buckling behaviour of a capsule enclosed by a thin wall, subjected to large displacements and deformations due to its interaction with the surrounding flow. The fluid flow is assumed to be inertialess on the capsule scale: this allows the use of the boundary integral formulation for the fluid velocity. Specifically, we would like to model a wall material that can be strain-hardening or softening, while accounting for the bending resistance due to a small but finite thickness. The shell model must allow the strong coupling between the solid (the wall dynamics) and fluid (the flow inside and outside the capsule) mechanics, remain stable, avoid numerical locking and keep the computational time tractable. We first discuss the different simplifications that are made when designing a shell model undergoing large deformations, and present the shear-membrane-bending model that allows for a nonlinear wall stretching law. We have chosen to illustrate the effect of bending resistance on a special case where bending effects are expected to be large: an ellipsoidal capsule subjected to a hyperbolic flow. The important results are that the coupling procedure is stable even when the capsule is undergoing very large deformations due to a strain-softening Neo-Hookean material constitutive law (NH), and that the post-buckling behaviour of the capsule depends on the material constitutive law.

The paper is organized as follows. Section 2 discusses the main simplifying hypotheses used to formulate a thin shell theory and presents the shear-membrane-bending shell model where any non-linear membrane law can be used to model the mid–surface behaviour of the capsule. The fluid-structure coupling is done in Section 3 and its numerical implementation is presented in Section 4. The simple case of an ellipsoidal capsule in plane extensional flow is analyzed in Section 5 and

(a) 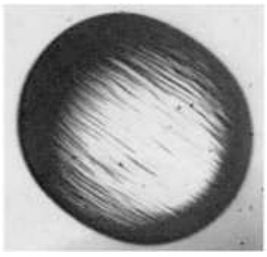 (b) 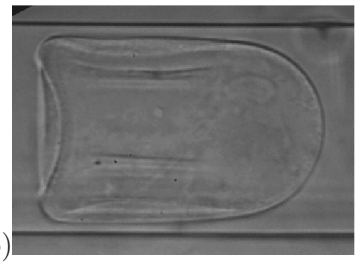 (c) 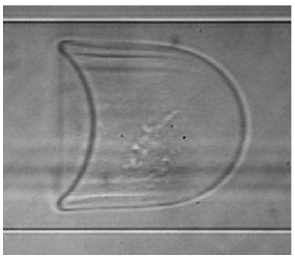

Figure 1: Experimental images of microcapsules deformed under hydrodynamic forces. (a) Polysiloxane microcapsule subjected to a simple shear flow (shear rate = 18 s^{-1}) (from Walter et al. [21]). (b) Alginate-ovalbumin microcapsule (2% (w/v) low viscosity alginate - 10% (w/v) ovalbumin, pH = 7.4, 15 min reticulation time) flowing in a cylindrical microchannel (radius of 75 μm) under a velocity of 13 mm/s and a capsule-to-tube confinement ratio of 1.09. (c) Ovalbumin microcapsule (10% (w/v) ovalbumin, pH = 7.4, 15 min reticulation time) flowing in a cylindrical microchannel (radius of 75 μm) under a velocity of 5.7 mm/s and a confinement ratio of 0.83. Images (b) and (c) were taken by Adlan Merlo (BMBI laboratory, UTC).

compared to those given by a pure membrane model.

2. Capsule wall mechanics

We present the main equations governing the motion and deformation of a capsule freely suspended in the flow of a Newtonian viscous liquid (viscosity μ, density ρ). The capsule is filled with a Newtonian incompressible liquid (viscosity μ, density ρ), enclosed by a thin wall made of an isotropic hyperelastic material having a bulk shear modulus G and a Poisson ratio ν in the limit of small deformation. Its characteristic size ℓ is defined as the radius of the sphere with the capsule volume V_c:

$$\ell = (3V_c/4\pi)^{1/3}. \tag{1}$$

The wall thickness $h = \alpha\ell$ is uniform and small compared to ℓ ($\alpha \ll 1$).

2.1. Curvilinear coordinate system

By convention, all quantities are denoted by capital letters in the reference initial state and by lowercase letters in the deformed state. Surface tensor components are denoted with Greek indices and three–dimensional tensor components with Latin indices. We adopt the Einstein summation convention on repeated indices.

Rather than treating the wall as a three–dimensional continuum, we take into account its thinness and use a shell theory [22], which consists of evaluating all quantities of interest on the wall

mid–surface $\mathcal{S}_t$ at time t. The position of a point in the shell is defined by three independent curvilinear coordinates (ξ^1, ξ^2, ξ^3). In the reference configuration, the position $\boldsymbol{X}$ of a material point within the capsule wall is then given by:

$$\boldsymbol{X}(\xi^1, \xi^2, \xi^3) = \boldsymbol{X}_s(\xi^1, \xi^2) + \xi^3 \boldsymbol{A}_3, \tag{2}$$

where $\boldsymbol{X}_s(\xi^1, \xi^2)$ is the position of a point M on the mid–surface $\mathcal{S}_0$ and where $|\xi^3|/\ell \leq \alpha/2$. A local surface covariant base $(\boldsymbol{A}_1, \boldsymbol{A}_2, \boldsymbol{A}_3)$ is then defined as:

$$\boldsymbol{A}_\alpha = \frac{d\boldsymbol{X}_s(\xi^1, \xi^2)}{d\xi^\alpha} = \boldsymbol{X}_{s,\alpha} \qquad \text{and} \qquad \boldsymbol{A}_3 = \frac{\boldsymbol{A}_1 \times \boldsymbol{A}_2}{\parallel \boldsymbol{A}_1 \times \boldsymbol{A}_2 \parallel}, \tag{3}$$

where $\boldsymbol{A}_3$ is the unit normal vector and where $_{,\alpha}$ denotes the partial derivation with respect to ξ_α. The contravariant base $(\boldsymbol{A}^1, \boldsymbol{A}^2, \boldsymbol{A}^3)$ is defined by $\boldsymbol{A}^\alpha \cdot \boldsymbol{A}_\beta = \delta^\alpha_\beta$ where δ^α_β is the Kronecker tensor and $\boldsymbol{A}^3 = \boldsymbol{A}_3$. The same quantities are defined in the deformed state using lowercase letters. Note that V_c corresponds to the volume enclosed by the wall mid–surface.

2.2. Wall deformation

In the deformed configuration, the new position $\boldsymbol{x}$ of a material point becomes:

$$\boldsymbol{x}(\boldsymbol{X}, t) = \boldsymbol{X} + \boldsymbol{u}(\boldsymbol{X}, t), \tag{4}$$

where $\boldsymbol{u}$ is the displacement field.

The variation of the distance between two points during deformation is measured by:

$$dx^2 - dX^2 = 2d\boldsymbol{X}^T \cdot \boldsymbol{e} \cdot d\boldsymbol{X} = 2d\boldsymbol{x}^T \cdot \boldsymbol{d} \cdot d\boldsymbol{x}. \tag{5}$$

The Green–Lagrange $\boldsymbol{e}$ and Euler-Almansi $\boldsymbol{d}$ strain tensors are defined by:

$$\boldsymbol{e} = \frac{1}{2}(\boldsymbol{F}^T \cdot \boldsymbol{F} - \boldsymbol{I}) = \boldsymbol{F}^T \cdot \boldsymbol{d} \cdot \boldsymbol{F}, \tag{6}$$

where $\boldsymbol{F} = \partial \boldsymbol{x}/\partial \boldsymbol{X}$ is the displacement gradient, with three positive singular values $\lambda_1, \lambda_2, \lambda_3$. Three independent invariants of $\boldsymbol{e}$ can be defined by:

$$\begin{aligned} I_1 &= tr(\boldsymbol{F}^T \cdot \boldsymbol{F}) - 3 = \lambda_1^2 + \lambda_2^2 + \lambda_3^2 - 3 \\ I_2 &= \frac{1}{2}\{[tr(\boldsymbol{F}^T \cdot \boldsymbol{F})]^2 - tr[(\boldsymbol{F}^T \cdot \boldsymbol{F})^2]\} = \lambda_1^2\lambda_2^2 + \lambda_2^2\lambda_3^2 + \lambda_3^2\lambda_1^2 - 3 \\ I_3 &= det(\boldsymbol{F}) - 1 = \lambda_1\lambda_2\lambda_3 - 1. \end{aligned} \tag{7}$$

When the capsule wall is made of a homogeneous, isotropic, hyperelastic material, the strain energy density W per unit volume of undeformed material depends only on the invariants of $\boldsymbol{e}$. The second Piola-Kirchhoff stress tensor $\boldsymbol{\Sigma}$ (pull back of forces per unit area in the undeformed reference configuration) and Cauchy stress tensor $\boldsymbol{\sigma}$ (forces per unit area in the deformed reference configuration) are given by:

$$\boldsymbol{\Sigma} = \frac{\partial W}{\partial \boldsymbol{e}}, \quad \boldsymbol{\sigma} = \frac{1}{det(\boldsymbol{F})} \boldsymbol{F} \cdot \boldsymbol{\Sigma} \cdot \boldsymbol{F}^T. \tag{8}$$

Different phenomenological constitutive laws can be postulated. The simplest one is the generalized Hooke's law (GH) in which a linear relation between $\boldsymbol{\Sigma}$ and $\boldsymbol{e}$ is postulated, which leads to:

$$W = G \left[tr(\boldsymbol{e}^2) + \frac{\nu}{1-2\nu} (tr\boldsymbol{e})^2 \right] = \frac{G}{4} \left[I_1^2 + 4I_1 - 2I_2 + \frac{\nu}{1-2\nu} I_1^2 \right], \tag{9}$$

and

$$\boldsymbol{\Sigma} = 2G \left[\boldsymbol{e} + \frac{\nu}{1-2\nu} tr\boldsymbol{e}\ \boldsymbol{I} \right], \tag{10}$$

where $\boldsymbol{I}$ is the identity tensor. Note that when the deformation is large, the Cauchy stress $\boldsymbol{\sigma}$ is a nonlinear function of $\boldsymbol{e}$.

2.3. Thin shell simplifications

When the shell is thin, a number of simplifying assumptions are classically made.

2.3.1. Plane stress assumption

The first one is to postulate that the main stresses in the shell are plane and tangent to the mid–surface. This corresponds to the assumption $\Sigma_{33} = \sigma_{33} = 0$ and implies that the membrane stresses in the mid–surface are prevalent. The three-dimensional constitutive law (10) reduces to:

$$\boldsymbol{\Sigma}_p = 2G \left[\boldsymbol{e} + \frac{\nu}{1-\nu} (e_{11} + e_{22}) \boldsymbol{I} \right], \tag{11}$$

In the local curvilinear coordinate system where we write $\boldsymbol{e} = e_{ij} \boldsymbol{A}^i \otimes \boldsymbol{A}^j$, $\boldsymbol{\Sigma}_p = \Sigma_p^{ij} \boldsymbol{A}_i \otimes \boldsymbol{A}_j$ and $\boldsymbol{A}^\alpha = A^{\alpha\beta} \boldsymbol{A}_\beta$, the components of $\boldsymbol{\Sigma}_p$ become:

$$\Sigma_p^{\alpha\beta} = C^{\alpha\beta\lambda\mu}\, e_{\lambda\mu}, \quad \Sigma_p^{\alpha 3} = \frac{1}{2} D^{\alpha\lambda}\, e_{\lambda 3}, \tag{12}$$

with

$$C^{\alpha\beta\lambda\mu} = G \left(A^{\alpha\lambda}\, A^{\beta\mu} + A^{\alpha\mu}\, A^{\beta\lambda} + \frac{2\nu}{1-\nu}\, A^{\alpha\beta}\, A^{\lambda\nu} \right), \quad D^{\alpha\lambda} = 4G\, A^{\alpha\lambda}. \tag{13}$$

2.3.2. Reissner–Mindlin kinematic simplification

The second simplification consists of postulating the form of the displacement within the shell thickness. For example, in the classical Reissner–Mindlin kinematic simplification [22], a material line initially orthogonal to the mid–surface remains undeformed during motion, but does not remain orthogonal to the deformed mid–surface. This means that shear deformations within the shell thickness are taken into account. The displacement field $\boldsymbol{u}$ is thus specified as:

$$\boldsymbol{u}(\xi^1,\xi^2,\xi^3,t) = \boldsymbol{u}_s(\xi^1,\xi^2,t) + \xi^3\,\boldsymbol{\theta}(\xi^1,\xi^2,t). \tag{14}$$

In the above, $\boldsymbol{u}_s(\xi^1,\xi^2,t)$ denotes the displacement of a point M of the mid–surface. The rotation surface vector is defined as $\boldsymbol{\theta}(\xi^1,\xi^2,t) = \theta_\lambda(\xi^1,\xi^2,t)\,\boldsymbol{a}^\lambda(\xi^1,\xi^2,t)$ where in the case of small rotation the angles θ_1 and θ_2 are the rotation angles of the normal vector to the mid–surface at M around vectors $\boldsymbol{a}_2$ and $\boldsymbol{a}_1$, respectively. As shown by Chapelle & Bathe [22] and Dupont [23], the components of $\boldsymbol{e}$ in the contravariant basis $(\boldsymbol{A}^1,\boldsymbol{A}^2,\boldsymbol{A}^3)$, are given by:

$$\left\{\begin{array}{lcl} e_{\alpha\beta} &=& \gamma_{\alpha\beta}(\boldsymbol{u}_s) + \xi^3\chi_{\alpha\beta}(\boldsymbol{u}_s,\boldsymbol{\theta}) + (\xi^3)^2\kappa_{\alpha\beta}(\boldsymbol{u}_s,\boldsymbol{\theta}),\\ e_{\alpha 3} &=& \zeta_{\alpha 3}(\boldsymbol{u}_s,\boldsymbol{\theta}),\\ e_{33} &=& 0. \end{array}\right. \tag{15}$$

The tensors $\gamma_{\alpha\beta}$, $\chi_{\alpha\beta}$ and $\kappa_{\alpha\beta}$ are the membrane strain, bending strain and curvature tensors respectively, while the vector $\zeta_{\alpha 3}$ is the shear strain vector. They are given by:

$$\gamma_{\alpha\beta} = \frac{1}{2}\left[\boldsymbol{A}_\alpha\cdot\boldsymbol{u}_{s,\beta} + \boldsymbol{A}_\beta\cdot\boldsymbol{u}_{s,\alpha} + \boldsymbol{u}_{s,\alpha}\cdot\boldsymbol{u}_{s,\beta}\right], \tag{16}$$

$$\chi_{\alpha\beta} = \frac{1}{2}[\boldsymbol{u}_{s,\alpha}\cdot\boldsymbol{A}_{3,\beta} + \boldsymbol{u}_{s,\beta}\cdot\boldsymbol{A}_{3,\alpha} + \boldsymbol{\theta}_{,\alpha}\cdot\boldsymbol{A}_\beta + \boldsymbol{\theta}_{,\beta}\cdot\boldsymbol{A}_\alpha + \boldsymbol{\theta}_{,\beta}\cdot\boldsymbol{u}_{s,\alpha} + \boldsymbol{\theta}_{,\alpha}\cdot\boldsymbol{u}_{s,\beta}] \tag{17}$$

$$\zeta_{\alpha 3} = \frac{1}{2}\left[\boldsymbol{A}_\alpha\cdot\boldsymbol{\theta} + \boldsymbol{A}_3\cdot\boldsymbol{u}_{s,\alpha} + \boldsymbol{\theta}\cdot\boldsymbol{u}_{s,\alpha}\right]. \tag{18}$$

$$\kappa_{\alpha\beta} = \frac{1}{2}\left[\boldsymbol{A}_{3,\alpha}\cdot\boldsymbol{\theta}_{,\beta} + \boldsymbol{A}_{3,\beta}\cdot\boldsymbol{\theta}_{,\alpha} + \boldsymbol{\theta}_{,\alpha}\cdot\boldsymbol{\theta}_{,\beta}\right]. \tag{19}$$

Note that in opposition with the linearized theory of Chapelle & Bathe [22], nonlinear terms (e.g. $\boldsymbol{u}_{s,\alpha}\cdot\boldsymbol{u}_{s,\beta}$) are retained in Eq. (16) to (19). This allows us to consider large transformations of the capsule wall. When shear deformations are neglected ($\zeta_{\alpha 3} = 0$), we recover the classical Kirchhoff-Love hypothesis, whereby the initial normal to the mid–surface remains normal to the deformed mid–surface.

2.3.3. Thin shell model vs. membrane model

When the wall is infinitely thin or when bending effects are ignored, the deformations in the membrane thickness are neglected ($\chi_{\alpha\beta} = 0$ and $\zeta_{\alpha 3} = 0$): we then recover the classical membrane model where the capsule wall is reduced to its mid–surface $\mathcal{S}_t$. The two–dimensional displacement gradient $\boldsymbol{F_s}$ and deformation tensor $\boldsymbol{e_s}$ are obtained from Eq. (4), (6) and (14) for $\xi^3 = 0$. In that case, the displacement gradient and membrane Cauchy-Green deformation tensors are simply:

$$\boldsymbol{F_s} = \frac{\partial(\boldsymbol{X}_s + \boldsymbol{u}_s)}{\partial \boldsymbol{X}_s}, \quad \boldsymbol{e_s} = \gamma_{\alpha\beta}\boldsymbol{A}^\alpha \otimes \boldsymbol{A}^\beta. \tag{20}$$

Two independent invariants of deformation can be defined:

$$I_{s1} = 2tr(\boldsymbol{e_s}), \quad I_{s2} = J_s - 1, \tag{21}$$

where $J_s = det(\boldsymbol{F_s})$. The invariant I_{s2} thus represents the relative surface area change during deformation. Integrating the plane strain energy W across the thickness leads to the strain energy per unit surface area W_s. The three-dimensional stress tensors are reduced to two-dimensional stress tensors $\boldsymbol{\Sigma_s}$ (pull back forces per unit length of curves in $\mathcal{S}_0$) and $\boldsymbol{\sigma_s}$ (forces per unit length of curves in $\mathcal{S}_t$):

$$\boldsymbol{\Sigma_s} = \frac{\partial W_s}{\partial \boldsymbol{e_s}}, \quad \boldsymbol{\sigma_s} = \frac{1}{det(\boldsymbol{F_s})}\boldsymbol{F_s} \cdot \boldsymbol{\Sigma_s} \cdot \boldsymbol{F_s}^T. \tag{22}$$

Correspondingly, the membrane version of the generalized Hooke's law is:

$$W_s = \frac{G_s}{4}\left[2I_{s1} - 2I_{s2} + \frac{1}{1-\nu_s}I_{1s}^2\right] \tag{23}$$

$$\boldsymbol{\Sigma_s} = 2G_s\left[\boldsymbol{e_s} + \frac{\nu_s}{1-\nu_s}tr(\boldsymbol{e_s})\boldsymbol{I}\right], \tag{24}$$

where $G_s = G\alpha\ell$ is the surface shear modulus and $\nu_s = \nu$ the surface Poisson ratio. The two material parameters G_s and ν_s can similarly be determined for any nonlinear membrane law in the limit of small deformations [24]. Note that the difference between Eq. (11) and Eq. (24) is that $\boldsymbol{\Sigma_p}$ is a three-dimensional stress tensor (forces per unit surface) with nine components whereas $\boldsymbol{\Sigma_s}$ is a two-dimensional tension tensor (force per unit length) with only four components.

2.4. Wall equilibrium: basic shell model

The wall equilibrium equations are then

$$\begin{cases} \nabla \cdot \boldsymbol{\sigma} = 0 \text{ inside the wall,} \\ \boldsymbol{\sigma} \cdot \boldsymbol{a}_3 = \boldsymbol{q}^+ \text{ on the external wall surface } \mathcal{S}_t^+, \\ \boldsymbol{\sigma} \cdot \boldsymbol{a}_3 = -\boldsymbol{q}^- \text{ on the internal wall surface } \mathcal{S}_t^-, \end{cases} \tag{25}$$

where $\boldsymbol{q}^+$ (respectively $\boldsymbol{q}^-$) is the load per unit deformed area. Using the virtual work principle, they can be written as:

$$\int_{\mathcal{S}_t^+} \hat{\boldsymbol{u}} \cdot \boldsymbol{q}^+ \, dS - \int_{\mathcal{S}_t^-} \hat{\boldsymbol{u}} \cdot \boldsymbol{q}^- \, dS = \int_{V_{wt}} \frac{\partial \hat{\boldsymbol{u}}}{\partial \boldsymbol{x}} : \boldsymbol{\sigma} \, dV, \tag{26}$$

where V_{wt} is the shell wall volume in the deformed state and $\hat{\boldsymbol{u}}(\hat{\boldsymbol{u}}_s, \hat{\boldsymbol{\theta}})$ any virtual displacement satisfying the Reissner–Mindlin assumption (Eq. 14). Since the capsule wall is thin, the virtual work of the load can be expressed in terms of a load $\boldsymbol{q}_s$ evaluated on the mid–surface. The Eulerian form of the equilibrium equation thus reads

$$\int_{\mathcal{S}_t} \hat{\boldsymbol{u}} \cdot \boldsymbol{q}_s \, dS = \int_{V_{wt}} \frac{\partial \hat{\boldsymbol{u}}}{\partial \boldsymbol{x}} : \boldsymbol{\sigma} \, dV = \int_{V_{wt}} \hat{\boldsymbol{d}} : \boldsymbol{\sigma} \, dV, \tag{27}$$

where $\hat{\boldsymbol{d}}$ is the virtual Euler-Almansi strain tensor. The right-hand-side of Eq. (27), which corresponds to the virtual work of the internal forces, can be evaluated in the wall volume in the undeformed state V_{w0} (Lagrangian form):

$$\int_{\mathcal{S}_t} \hat{\boldsymbol{u}} \cdot \boldsymbol{q}_s \, dS = \int_{V_{w0}} \hat{\boldsymbol{e}} : \boldsymbol{\Sigma} \, dV, \tag{28}$$

where $\hat{\boldsymbol{e}}$ is the linearized Green-Lagrange virtual strain tensor, corresponding to the virtual displacement $\hat{\boldsymbol{u}}(\hat{\boldsymbol{u}}_s, \hat{\boldsymbol{\theta}})$. Its components are given by linearizing Eq. (15) along the directions $\hat{\boldsymbol{u}}_s$ and $\hat{\boldsymbol{\theta}}$, respectively. The basic shell model [22] corresponds to Eq. (28) and (6) and describes the mechanical equilibrium of a thin shell made of a Hookean material (Eq. 11), under the condition of plane stress and a Reissner–Mindlin displacement field.

2.5. Shear-membrane-bending models (SMB)

In order to facilitate the shell computation, it is useful to simplify further the basic shell model and decouple the respective contributions to the wall equilibrium, of the mid-surface membrane deformation, of the bending moments and of the shear deformations within the wall thickness. In order to achieve this, the higher order terms in $(\xi^3)^2$ are neglected in the components of $\boldsymbol{e}$ (Eq. 15).

Evaluating the right-hand-side term of the equlibrium equation (28) for the case where $\boldsymbol{\Sigma}$ is given by the simplified generalized Hooke's law (Eq. 11), we obtain :

$$\begin{aligned} \int_{\mathcal{S}_t} \hat{\boldsymbol{u}} \cdot \boldsymbol{q}_s \, dS &= \int_{V_0} C^{\alpha\beta\lambda\mu} \left(\gamma_{\alpha\beta} + \xi^3 \chi_{\alpha\beta}\right) \left(\hat{\gamma}_{\lambda\mu} + \xi^3 \hat{\chi}_{\lambda\mu}\right) \, dV \\ &+ \int_{V_0} D_s^{\alpha\lambda} \, \zeta_{\alpha 3} \, \hat{\zeta}_{\lambda 3} \, dV. \end{aligned} \tag{29}$$

We then integrate across the thickness to obtain:

$$\begin{aligned}\int_{\mathcal{S}_t} \hat{\boldsymbol{u}} \cdot \boldsymbol{q}_s \, dS &= \int_{\mathcal{S}_0} hC^{\alpha\beta\lambda\mu} \left[\gamma_{\alpha\beta} \, \hat{\gamma}_{\lambda\mu} + \frac{h^2}{12} \, \chi_{\alpha\beta} \, \hat{\chi}_{\lambda\mu} \right] dS \\ &+ \int_{\mathcal{S}_0} hD^{\alpha\lambda} \, \zeta_{\alpha 3} \, \hat{\zeta}_{\alpha 3} \, dS. \end{aligned} \tag{30}$$

Equation (30) relates the load $\boldsymbol{q}_s$ on a thin shell to the 2D membrane stresses in the mid–surface ($hC_s^{\alpha\beta\lambda\mu} \, \gamma_{\alpha\beta}$), shear stress ($hD_s^{\alpha\lambda} \, \zeta_{\alpha 3}$) and bending stress $h^3/12 \, C_s^{\alpha\beta\lambda\mu} \, \chi_{\alpha\beta}$. Since all non linear terms have been kept in the construction of the membrane, shear and bending strain in Eq. (16, 17, 18), Eq. (30) applies for large transformations and constitutes a generalization of the classical shear-membrane-bending (SMB) theory, which was derived for small elastic deformation [22].

2.6. Generalized shear-membrane-bending model (GSMB)

The above model (Eq. 30) adds a bending resistance to the wall model of the capsule, but the underlying membrane model is based on generalized Hooke's law, whose strain-hardening behaviour might not be adequate for the constitutive wall material. We therefore propose a generalization of this model that accounts for more general underlying membrane models. We begin by noting that the stress term $hC^{\alpha\beta\lambda\mu} \, \gamma_{\alpha\beta}$ can also be interpreted as the stress $\boldsymbol{\Sigma_s} = \partial W_s / \partial \boldsymbol{e}_s$ in a membrane that satisfies Hooke's law (Eq. 23). We thus propose to rewrite Eq. (30) as

$$\begin{aligned}\int_{\mathcal{S}_t} \hat{\boldsymbol{u}} \cdot \boldsymbol{q}_s \, dS &= \int_{\mathcal{S}_0} \frac{\partial W_s}{\partial \gamma_{\lambda\mu}} \hat{\gamma}_{\lambda\mu} dS \\ &+ \int_{\mathcal{S}_0} C_s^{\alpha\beta\lambda\mu} \frac{h^3}{12} \, \chi_{\alpha\beta} \, \hat{\chi}_{\lambda\mu} dS \\ &+ \int_{\mathcal{S}_0} hD_s^{\alpha\lambda} \, \zeta_{\alpha 3} \, \hat{\zeta}_{\alpha 3} \, dS, \end{aligned} \tag{31}$$

and interpret W_s now as the energy density of any membrane constitutive law. This generalized shear-membrane-bending model (GSMB) thus allows us to consider any nonlinear hyperelastic membrane behaviour, with small deformation values of the shear and surface Poisson ratio denoted by G_s and ν_s, respectively. However, the bending and shear behaviour of the wall are computed by means of the linear Hooke's law, with values of material parameters $G = G_s/h$ and $\nu = \nu_s$.

For example, consider a capsule wall made of an incompressible material (typically an elastomer or a gel) that obeys a neo-Hookean (NH) type law, i.e. a simple version of the Mooney-Rivlin law.

The three-dimensional strain energy is given by

$$W^{NH} = \frac{G}{2} I_1, \tag{32}$$

which reduces after integration across the wall thickness to the membrane strain energy

$$W_s^{NH} = \frac{G_s}{2} \left[I_{s1} - 1 + \frac{1}{I_{s2} + 1} \right], \tag{33}$$

with $\nu = \nu_s = 1/2$, in view of the material incompressibility. Under uniaxial extension and large deformations, the neo-Hookean law (Eq. 33) predicts a strain-softening behaviour of the wall, whereas the generalized Hooke's law (Eq. 23) predicts a strain-hardening behaviour (typical of a wall made of a cross-linked polymer network). Thus the great advantage of the GSMB model is that it allows us to consider capsules with walls made of different materials. Of course, it would be possible to use a basic shell model provided that we could identify not only the in plane behaviour of the constitutive material but also its full 3D nonlinear strain energy density. For soft materials, we would moreover be faced with the additional complexity of introducing an enriched 3D kinematics [25] because the standard Reissner–Mindlin assumption fails to reproduce the local transverse response of the material across its thickness. The advantage of the GSMB simplification is that the transverse effects (shear and bending) are linearized in deformation, which is reasonable for capsule problems with limited bending forces. Moreover, the mechanical coefficients are simpler to identifiy and the model stays cost efficient in terms of computational time.

3. Capsule dynamics in flow

3.1. General case

We assume that the capsule is small, so that the Reynolds number $Re = \mu V \ell / \rho$ is small, where V is the characteristic dimension of the flow velocity. The flow inside and outside the capsule is thus governed by the Stokes equations. In principle, the flow boundary conditions should be written separately for $\mathcal{S}_t^+$ and $\mathcal{S}_t^-$. However, to remain consistent with the thin shell approximations, we write them on the wall mid–surface. Correspondingly, the boundary integral expression of the flow velocity is given by

$$\boldsymbol{v}(\boldsymbol{x}_s) = \boldsymbol{v}^{\infty}(\boldsymbol{x}_s) - \frac{1}{8\pi\mu} \int_{\mathcal{S}_t} \left(\frac{\boldsymbol{I}}{\| \boldsymbol{r} \|} + \frac{\boldsymbol{r} \otimes \boldsymbol{r}}{\| \boldsymbol{r} \|^3} \right) \cdot \boldsymbol{q}_s(\boldsymbol{y}_s) \, dS, \tag{34}$$

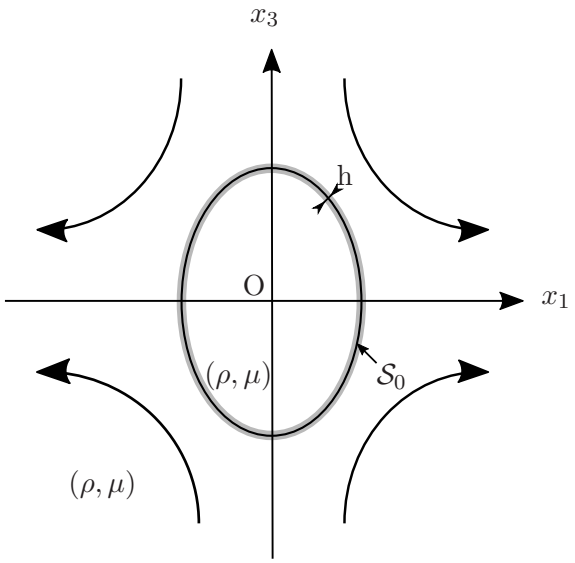

Figure 2: Schematic illustration of an initially ellipsoidal capsule placed in a plane hyperbolic flow.

where $\boldsymbol{v}^\infty$ is the undisturbed flow velocity and $\boldsymbol{r} = \boldsymbol{x}_s - \boldsymbol{y}_s$. The wall and fluid motions are coupled through the load $\boldsymbol{q}_s$ that appears in Eqs. (34) and (31) and through the no-slip condition that requires

$$\boldsymbol{v}\left(\boldsymbol{x}_s(\xi^1, \xi^2, t)\right) = \frac{\partial}{\partial t}\, \boldsymbol{u}_s(\xi^1, \xi^2, t). \tag{35}$$

The main problem parameters are the relative wall thickness α associated to the ratio between the bending stiffness $G\alpha^3 l^3/12$ and the shear surface modulus $G_s = G\alpha l$, the wall Poisson ratio ν and the bulk capillary number

$$Ca_v = \mu\dot{\gamma}/G, \tag{36}$$

which compares the viscous to the elastic forces. For an infinitely thin wall, described by a membrane model, a surface capillary number is used

$$Ca_s = \mu\dot{\gamma}\ell/G_s = Ca_v/\alpha. \tag{37}$$

3.2. Ellipsoidal capsule in a plane hyperbolic flow

The GSMB approximation is tested on the case of a capsule which is an axisymmetric prolate ellipsoid in the reference state (Figure 2). In a reference frame $(\boldsymbol{e}_1, \boldsymbol{e}_2, \boldsymbol{e}_3)$ centered on the ellipsoid centre, the equation of $\mathcal{S}_0$ is given by

$$X_{s1}^2/b^2 + X_{s2}^2/b^2 + X_{s3}^2/a^2 = 1, \tag{38}$$

where a is the long axis and b the equator radius. The length scale ℓ is thus $\ell = (ab^2)^{1/3}$.

At time $t = 0$, the ellipsoid is freely suspended in a plane hyperbolic flow given by

$$\boldsymbol{v}^{\infty}(\boldsymbol{x}) = \dot{\gamma}(x_1\boldsymbol{e}_1 - x_3\boldsymbol{e}_3). \tag{39}$$

Under the influence of the viscous forces, the capsule wall is stretched in the x_1-direction and compressed in the x_3-direction. The small and large axes are exchanged: the longest axis, which was initially along x_3, may be along x_1 in the steady deformed state. As a consequence, we can expect large deformations and large curvature changes: this is a good test case to study the predictions of the GSMB theory and analyze the influence of the wall thickness on the capsule motion and deformation. Correspondingly, we will monitor the time evolution of the deformation of a capsule when it is suddenly subjected to a hyperbolic flow at time $t = 0$. The profile distortion will be quantified by the steady Taylor deformation $D_{ij}(t)$

$$D_{ij}(t) = \frac{Le_i(t) - Le_j(t)}{Le_i(t) + Le_j^{(}t)} \tag{40}$$

where Le_i and Le_j are the lengths, in the x_ix_j-plane, of the principal axes of the ellipsoid of inertia of the mid–surface $\mathcal{S}_t$. Unless otherwise mentioned, we concentrate on one ellipsoidal shape for which $a/b = 1.4$, corresponding to $D_{13}(0) = D_{23}(0) = -0.17$ and $D_{12}(0) = 0$.

4. Numerical method and validation

4.1. Numerical scheme

The numerical procedure was outlined by Dupont et al. [18], who used the basic shell model to describe the capsule wall. We thus only present the main procedure and discuss how the solid solver differs from a standard finite element scheme. The fluid–structure problem is solved by coupling (i) a shell finite element method to compute the load $\boldsymbol{q}_s$ corresponding to a given mid–surface displacement $\boldsymbol{u}_s$ and (ii) a boundary integral method to compute the local velocity of the mid–surface points for a given deformed capsule geometry and load $\boldsymbol{q}_s$. The two solvers are used in succession: for a given load $\boldsymbol{q}_s$ transmitted by the solid solver, the velocity field $\boldsymbol{v}_s(\boldsymbol{X}, t)$ is computed by the fluid solver and integrated in time to yield the position $\boldsymbol{u}_s$ of the mid–surface. The updated displacement field $\boldsymbol{u}_s$ is then transfered to the solid solver which computes the load $\boldsymbol{q}_s$ and transfers it to the fluid solver. Note that whereas the calculation of $\boldsymbol{q}_s$ is explicit for a membrane model, we

have to solve an equilibrium model to compute the rotation field $\boldsymbol{\theta}$ for the shell model at each time step, which lengthens the solid computation. The process stops when a steady-state is reached, i.e. when the capsule area varies by less than $5 \times 10^{-4}(4\pi\ell^2)$ over a non-dimensional time $\dot{\gamma}t = 1$.

The explicit nature of the time integration scheme makes it unstable unless the time steps Δt, between two successive iterations satisfies the stability criterion [26]:

$$\dot{\gamma}\Delta t < \mathcal{O}\left(\frac{\Delta x\, Ca_v}{h}\right), \tag{41}$$

where Δx is the mesh size.

The undeformed mid–surface of the capsule wall is discretized with MITC3 elements (triangular shell elements with three nodes using the Mixed Interpolation Tensorial Components technique of [27]). Correspondingly, an icosahedron (regular polyhedron with 20 triangular faces) is inscribed in a sphere with radius $\ell = 1$. Its triangular faces are sequentially subdivided and the resulting nodes are projected on the sphere. The spherical grid is then transformed into an ellipsoidal grid by means of a straightforward affine transformation. We use 2562 nodes corresponding to 5120 elements and an average mesh size $\Delta x/\ell = 0.075$. The time step is $\dot{\gamma}\Delta t = 10^{-4}$.

For a given MITC3 element, $\lambda^{(p)}$ denotes the standard linear shape function associated with node $p \in \{1, 2, 3\}$. In the following, we note $f_j^{(p)}$ the value of the j^{th} Cartesian component of any vector $\boldsymbol{f}$ at node p. The local Cartesian coordinates system (r, s, z) is defined for each element, where (r, s) are the intrinsic coordinates in the plane element (defined such that r, s and $1 - r - s \in [0, 1]$) and z is the coordinate along the deformed normal vector $\boldsymbol{a}_3$ ($z \in [-1, 1]$). The position $\boldsymbol{x}$ and the corresponding virtual displacement $\hat{\boldsymbol{u}}$ inside the given element are then expressed as

$$\boldsymbol{x}(t) = \sum_{p=1}^{3} \lambda^{(p)}(r, s)\left(\boldsymbol{x}_s^{(p)}(t) + z\,\frac{\alpha\ell}{2}\,\boldsymbol{a}_3^{(p)}(t)\right), \tag{42}$$

$$\hat{\boldsymbol{u}} = \sum_{p=1}^{3} \lambda^{(p)}(r, s)\left(\hat{\boldsymbol{u}}_s^{(p)} + z\,\frac{\alpha\ell}{2}\,\hat{\boldsymbol{\theta}}^{(p)}\right). \tag{43}$$

For the sake of simplicity, we will provide the algebraic expression of the finite element formulation for the basic shell model (Eq. 28). The left–hand side of Eq. (28) is calculated on the deformed state:

$$\int_{\mathcal{S}_t} \hat{\boldsymbol{u}} \cdot \boldsymbol{q}\, dS = \sum_{el} \hat{u}_j^{(p)} \left(\int_{\mathcal{S}_{el}} \lambda^{(p)}\lambda^{(q)} dS\right) q_j^{(q)} = \{\hat{u}\}^T\,[M]\,\{q\}. \tag{44}$$

It results from the assembling of each elementary vector of the discrete virtual displacement $\{\hat{u}\}$ and load $\{q\}$ and of the matrix M, which contains the terms into brackets with the shape functions.

Similarly, the integral on the right–hand side of equation (28) is calculated on each individual element and summed over all the elements of the capsule surface. According to the definition of the Green–Lagrange strain tensor, the elementary vector $[e_{el}]$ can be written as $[e_{el}] = [B_{el}]\{u_{el}\}$, where $[B_{el}]$ is a matrix that contains the values of the partial derivatives calculated on the element [28, 29]. The right–hand side of equation (28) then becomes

$$\begin{aligned} \int_{V_{w0}} \hat{\boldsymbol{e}} : \boldsymbol{\Sigma}\, dV &= \sum_{el} \int_{V_{w0}} \{\hat{u}_{el}\}^T [B_{el}]^T [\Sigma_{el}]\, dV && (45) \\ &= \sum_{el} \{\hat{u_{el}}\}^T \{R_{el}\} && (46) \\ &= \{\hat{u}\}^T \{R\} && (47) \end{aligned}$$

where $\{R_{el}\}$ is the internal load vector inside the element, and where the vectors $\{\hat{u}_{el}\}$ and $\{R_{el}\}$ are assembled into their global counterparts in the final step.

After equating Eq. (44) and Eq. (47) and simplifying by $\{\hat{u}\}^T$, the discretized form of Eq. (28) becomes

$$[M]\{q\} = \{R\}(\{u_s\}, \{\theta\}). \tag{48}$$

The wall equilibrium discrete equations thus depend on the known degrees of freedom $\{u_s\}$ of the mid–surface displacement (computed by integrating the mesh nodes velocity provided by the fluid solver at the previous time step) and the unknown rotational degrees of freedom $\{\theta\}$, which can be calculated separately, if one rewrites the problem in the following form:

$$\begin{cases} \{R\}_s(\{u_s\}, \{\theta\}) - [M]_s\{q_s\} = \{0\}_s, & (49a) \\ \{R\}_\theta(\{u_s\}, \{\theta\}) = \{0\}_\theta. & (49b) \end{cases}$$

The viscous load $\{q_s\}$ is the second unknown in this system. To solve it, we first solve the nonlinear equation (49b) in $\{\theta\}$ by a Newton's method. Numerically, we define the residual of equation (49b) as

$$\mathcal{R}(\{\theta\}) = \{R\}_\theta(\{u_s\}, \{\theta\}). \tag{50}$$

We search for the rotations $\{\theta\}$ such that $\mathcal{R} = 0$. The equation is solved by subiterations (index i) setting the convergence criterion at 1×10^{-7}. Let $\{\theta^t\}$ be the rotation vector that satisfies the

zero–residual condition at time t and $\{\theta^{t+\Delta t}\}$ the solution that we are looking for at time $t+\Delta t$. As rotation initial guess $\{\theta_0^{t+\Delta t}\}$, we use the rotation found at the previous time step. Using a first–order Taylor series, one can express the residual at subiteration $i+1$ as

$$\mathcal{R}(\{\theta_{i+1}^{t+\Delta t}\}) = \mathcal{R}(\{\theta_i^{t+\Delta t}\}) + \frac{\partial \mathcal{R}(\{\theta_i^{t+\Delta t}\})}{\partial\{\theta\}} \left(\{\theta_{i+1}^{t+\Delta t}\} - \{\theta_i^{t+\Delta t}\}\right). \tag{51}$$

Let us search for $\{\theta_{i+1}^{t+\Delta t}\}$, such that $\mathcal{R}(\{\theta_{i+1}^{t+\Delta t}\}) = 0$. From equation (51), it reads

$$\begin{aligned} \{\theta_{i+1}^{t+\Delta t}\} &= \{\theta_i^{t+\Delta t}\} - \left[\frac{\partial \mathcal{R}(\{\theta_i^{t+\Delta t}\})}{\partial\{\theta\}}\right]^{-1} \mathcal{R}(\{\theta_i^{t+\Delta t}\}) \\ &= \{\theta_i^{t+\Delta t}\} - \left[K(\{\theta_i^{t+\Delta t}\})\right]^{-1} \mathcal{R}(\{\theta_i^{t+\Delta t}\}), \end{aligned} \tag{52}$$

where $[K]$ represents the stiffness matrix. Equation (52) is solved for explicitly, since $[K(\theta_i^{t+\Delta t})]$ and $\mathcal{R}(\theta_i^{t+\Delta t})$ are known from subiteration i. If the new solution does not respect the convergence criterion

$$|\{\theta_{i+1}^{t+\Delta t}\} - \{\theta_i^{t+\Delta t}\}| < 10^{-7}, \tag{53}$$

one has to move on to the next subiteration and iterate until convergence. Once the value of the rotation $\{\theta\}$ is found, the load $\{q_s\}$ exerted by the fluids on the wall is obtained by direct inversion of equation (49a).

The shell finite element code uses Shelddon libraries, designed by Inria[2]. The latter were modified to solve the solid problem (i) with the displacement as an input and (ii) for any material law for membrane effects. The global structure of the numerical scheme remains unchanged but the following changes are made:

- The subroutine to solve Eq. (49a) is modified to determine $\{q_s\}$, the classical unknown being the load $\{u_s\}$.
- The coupled terms and the terms corresponding to the curvature tensor $\boldsymbol{\kappa}_{\alpha\beta}$ are set to zero.
- The terms in α^2 are neglected.

[2]The Shelddon library is registered at the *Agence pour la Protection des Programmes* (ref IDDN.FR.001.030018.000.S.P.2010.000.20600). The base of the program is open source and available online: www-rocq.inria.fr/modulef.

- The structure of the matrix $[\Sigma_{el}]$ is modified to decouple the shear, bending and membrane effects and to select a constitutive law to govern membrane deformation.

In order to compute the load $\boldsymbol{q}_s$ using a Lagrangian tracking scheme, the Shelddon library is coupled with the fluid solver developed in the Biomechanics and Bioingineering Laboratory [7, 26, 30] using a Parallel Virtual Machine protocol. The velocity field is then obtained explicitly from Eq. (34), which is discretized on the mesh described above. Equation (35) is integrated by means of an explicit second-order Runge-Kutta method to compute $\boldsymbol{u}_s$. The updated displacement $\boldsymbol{u}_s$ is given back to the solid solver at the beginning of the following time loop.

4.2. Validation of the GSMB model

Dupont et al. [18] applied the basic shell model to an initially spherical capsule with a GH wall freely suspended in a simple shear flow. They showed that for high shear rates and any thickness, the predictions of the shell model are the same as those of the well documented membrane model, because stretching of the mid–surface is then the dominant phenomenon. This indicates that the basic shell model leads to validated predictions of the capsule deformed profile.

They also conducted a full convergence analysis that showed that the numerical coupled procedure converges as $(\Delta x/\ell)^2$ and $\dot{\gamma}\Delta t$. The GSMB numerical scheme, being based on the same numerical procedures, has the same temporal and spatial convergence. With the 5120 element mesh, we thus expect a precision of order 8×10^{-3} on the capsule Taylor deformation D_{ij}.

To validate the GSMB model, we now analyze the influence of the GSMB simplification. The motion of an initially prolate capsule, subjected to a hyperbolic flow (Eq. 39) for $Ca_v = 0.003$, is simulated using both the basic shell model (Eq. 28) and the GSMB model (Eq. 31), where W_s is given by the generalized Hooke's law (Eq. 23), which corresponds to the SMB model (Eq. 30). The two computations are done with the same 5120 elements mid-surface mesh and the same time step. In order to compare the results, we compute the distance $H(t)/\ell$ between two corresponding nodes of the deformed mid-surfaces obtained at steady state ($\dot{\gamma}t = 5$) with the two numerical schemes. Figure 3 shows the capsule deformed shape for two values of thickness ($\alpha = 3\%$ and 10%) as well as the mapping of the distance $H(t)/\ell$ over the capsule wall. For $\alpha = 3\%$, the capsule undergoes a large deformation with its long axis along the x_1-direction, while part of the capsule wall buckles. The maximum values of $H(t)/\ell$ are then of order $0.004 - 0.005$ and are found in the vicinity of the folds (Figure 3a). For $\alpha = 10\%$, there is no buckling and the maximum distance $H(t)/\ell$ is less than 0.001

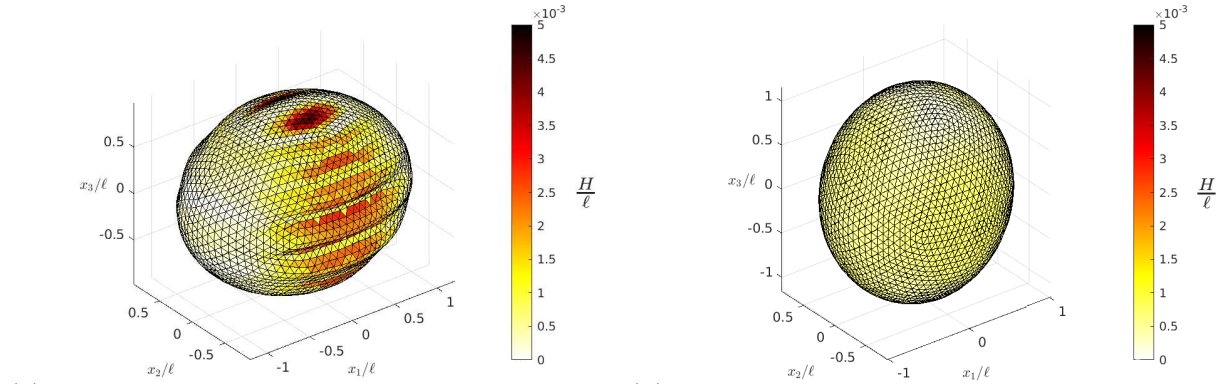

Figure 3: Steady state mapping of the distance H/ℓ between the basic shell model and the GSMB model (GH law) for $Ca_v = 0.003$ and $\dot{\gamma}t = 5$. (a) For $\alpha = 3\%$, the largest profile difference occurs in the buckled region; (b) For $\alpha = 10\%$, there no buckling and the profile difference is very small.

(Figure 3b). Altogether, the profile difference is very small and of the same order of magnitude as the precision of the numerical scheme. This validates the use of the GSMB simplification to model the capsule response, even when the deformation is large.

We now assess the influence of the mesh on the post-buckling behaviour by comparing the results obtained with the 5120 elements mesh to those obtained with a different mesh based on an octahedron (regular polyhedron with 8 triangular faces) and containing 8192 elements. For $Ca_v = 0.003$ and $\alpha = 3\%$, the maximum distance $H(t)/\ell$ is less than 0.03, which proves that the post-buckling behaviour is not affected by a change in the mesh geometry.

5. Results

5.1. Typical time evolution of a capsule

As an illustration we show the detailed time response of a capsule for $Ca_v = 0.003$ and $\alpha = 3\%$ when the wall obeys the GH law (Figure 4). Under the influence of the flow, the capsule is progressively stretched in the x_1-direction and compressed in the x_3-direction. The profile in the x_1x_3-plane evolves smoothly until a steady shape is reached (Figure 4b). As expected, the small and large axes are exchanged. If we analyze only the profile in the flow plane (x_1x_3), we might conclude that a steady state is reached for $\dot{\gamma}t \geq 1$ (Figure 4a). However, the deformation process is asymmetric: indeed, compression along the x_3-direction leads to buckling, as evidenced by the folds that appear on the surface of the capsule for $\dot{\gamma}t \geq 1$ (Figures 4a, c). It follows that the

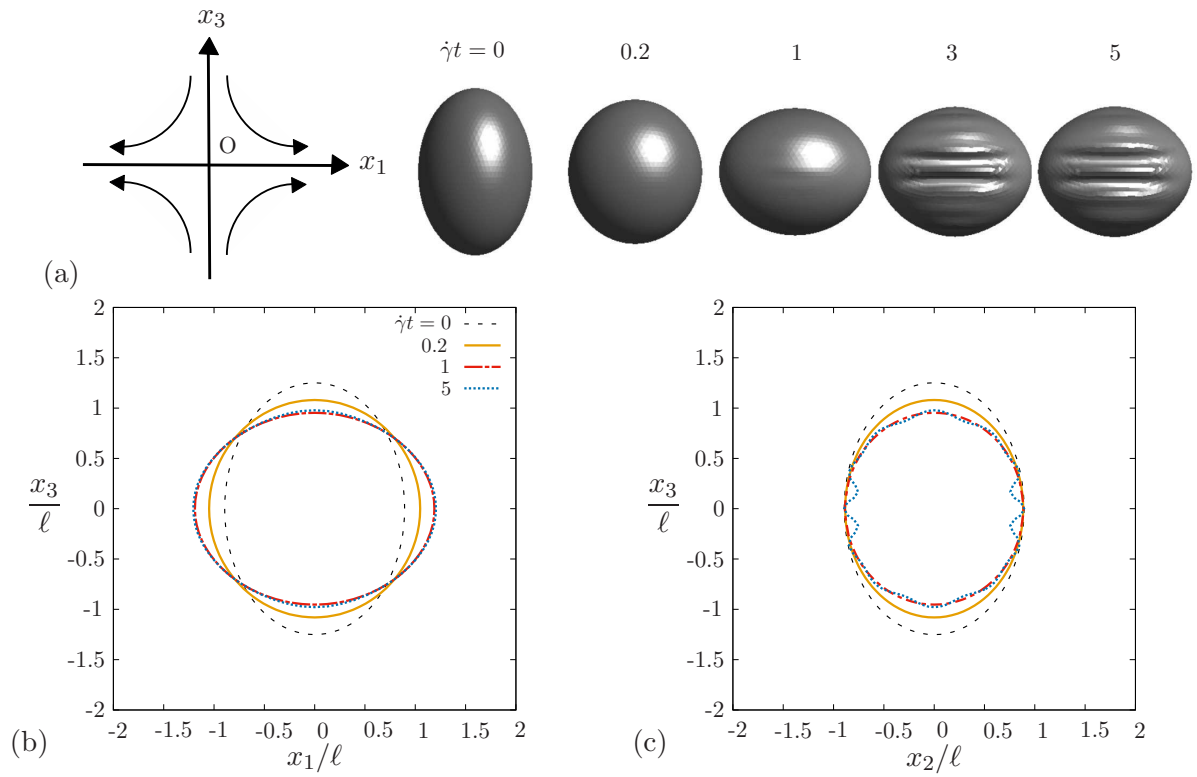

Figure 4: Temporal shape evolution of an initially prolate capsule subjected to a planar hyperbolic flow at $a/b = 1.4, Ca_v = 0.003, \alpha = 3\%$: (a) 3D view (the white spots are a lighting artefact), (b) ($\mathbf{e}_1$, $\mathbf{e}_3$)-plane, (c) ($\mathbf{e}_2$, $\mathbf{e}_3$)-plane. The GSMB model is used where the mid–surface deformation is governed by the generalized Hooke's law.

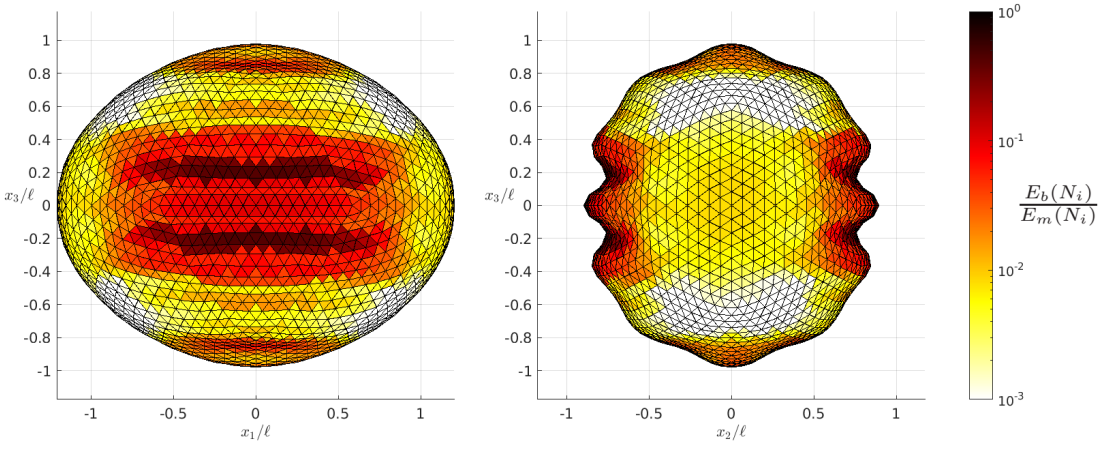

Figure 5: Mapping of the bending to membrane energy ratio $E_b(N_i)/E_m(N_i)$ at steady state ($\dot{\gamma}t = 5$) in (a) the flow plane (x_1x_3) and (b) the cross plane (x_2x_3). Same conditions as in Figure 4.

steady state is actually reached for $\dot{\gamma}t \sim 5$, when the folds have stabilized. The local distribution of membrane and bending energy at each node is defined as

$$E_m(N_i) = \frac{1}{\sum \Delta S_i} \sum \int_{\Delta S_i} W_s dS, \tag{54}$$

$$E_b(N_i) = \frac{1}{\sum \Delta S_i} \sum \int_{\Delta S_i} C_0^{\alpha\beta\lambda\mu} \frac{h^3}{12} \chi_{\alpha\beta} \chi_{\lambda\mu} dS \tag{55}$$

$$E_{sh}(N_i) = \frac{1}{\sum \Delta S_i} \sum \int_{\Delta S_i} h D_0^{\alpha\lambda} \zeta_{\alpha 3} \zeta_{\alpha 3} \, dS, \tag{56}$$

where ΔS_i is the surface of an element and where the sums are taken over the elements that share node N_i. The mapping of $E_b(N_i)/E_m(N_i)$ is shown in Figure 5, where a logarithmic scale is used to dampen out the effect of numerical errors in the computation of the bending energy and indicate the areas where bending effects are negligible. It appears clearly that bending and membrane effects have the same order of magnitude in the buckled areas only, whereas in the stretched areas, bending effects are negligible compared to membrane stretching forces. The differences of the bending-to-membrane energy ratio between the crest and trough of the wrinkles are due to variations in membrane energy, the bending one remaining constant. The shear to membrane local energy ratio, $E_{sh}(N_i)/E_m(N_i)$, is less than 0.03 everywhere (not shown).

5.2. Influence of Ca_v

The influence of the relative flow strength Ca_v on the capsule deformation is shown in Figure 6 for $\alpha = 3\%$. The elongation of the capsule in the flow direction increases with Ca_v (Figure 6a). The corresponding Taylor deformation at steady state D_{13}^{∞} also increases with Ca_v, and levels off for large values of Ca_v because the GH law is strain hardening (Figure 7a). The change in sign of D_{13}^{∞} is due to the fact that the long and short axes are interchanged.

As the flow strength increases (e.g. $Ca_v \geq 0.0075$ for $\alpha = 3\%$), the stretching energy of the mid–surface is large and bending energy becomes negligible by comparison. It can be expected, for those large values of Ca_v, that a simple membrane model where bending is ignored would be sufficient to compute the capsule deformation (see section 2.3.3).

5.3. Influence of the wall bending resistance

We analyze the effect of the wall bending resistance, as measured by α, on the capsule steady deformation for $Ca_v = 0.003$. The capsule mid–surface profiles in the flow plane (x_1, x_3) show

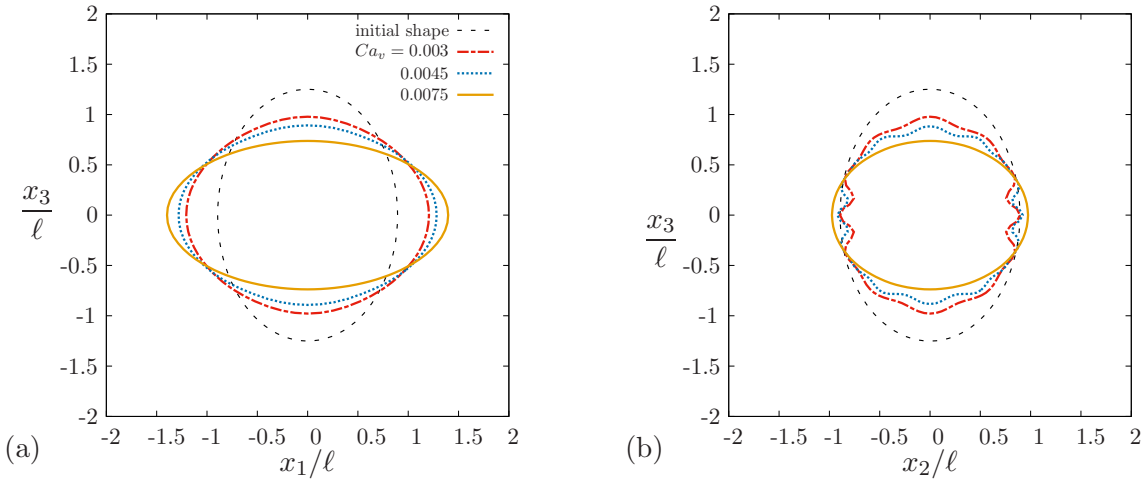

Figure 6: Influence of Ca_v on the capsule mid–surface deformation at steady-state ($\dot{\gamma}t = 5$, $\alpha = 3\%$, GH law). Mid–surface cross profiles in the flow plane (a) and in the perpendicular plane (b).

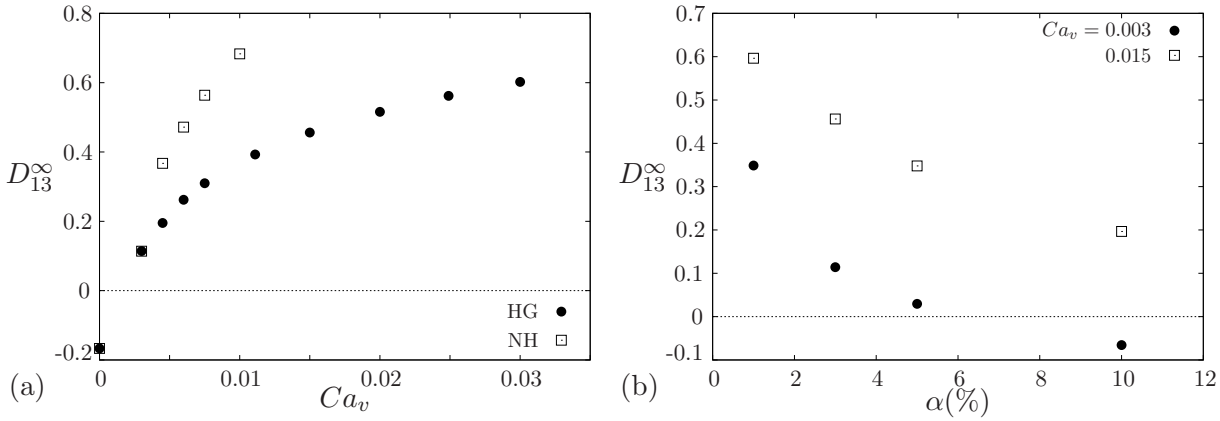

Figure 7: Steady state values of mid–surface Taylor deformation D_{13}^{∞}: (a) influence of flow strength and mid–surface constitutive law for $\alpha = 3\%$; (b) influence of bending resistance for low and high flow strength (GH law).

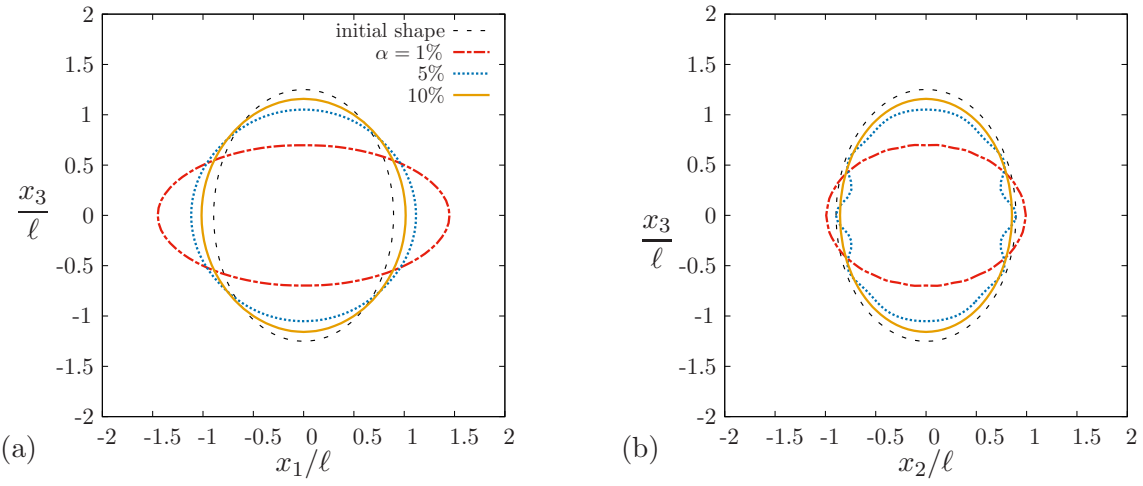

Figure 8: Influence of α on the capsule mid–surface at steady-state ($Ca_v = 0.003$, GH law). Mid–surface cross profiles in the flow plane (a) and in the perpendicular plane (b).

that the capsule becomes less elongated along x_1 as α increases (Figure 8a). Consequently the deformation D_{13}^{∞} decreases with increasing bending resistance (Figure 7b). In the cross plane, the situation is complex: for small wall values ($\alpha = 1\%$), the tensile stress level is such that the wall does not buckle (Figure 8b). However, for intermediate values $5\% \leq \alpha \leq 7.5\%$, the wall buckles because the overall deformation and tensile stresses of the capsule are too small ($D_{13}^{\infty} < 0.2$) to overcome the compressive stresses. The process is similar to the one that occurs for low Ca_v and $\alpha = 3\%$. For a large value $\alpha = 10\%$, the reduced deformation and low tensile stress level do not result in buckling because the bending resistance is large. It follows that the bending model of a shell allows us to study the complex balance between bending resistance, deformation and buckling.

For high flow strengths, e.g. $Ca_v = 0.015$, we recover the fact that the deformation D_{13}^{∞} decreases with wall thickness (Figure 7b). However as the capsule is more deformed, the wall does not buckle even when the thickness is small (Figure 9).

5.4. Influence of the mid–surface constitutive law

We now consider a strain-softening wall material that satisfies the neo-Hookean constitutive law (Eq. 32). We thus replace W_s in Eq. (31) by W_s^{NH} given by Eq. (33). As in section 5.2, the wall thickness ratio α is fixed to 3% and the effect of Ca_v is analyzed. We find again that the higher Ca_v is, the more elongated the capsule is in the flow direction (Figure 10a). This is confirmed by the evolution of the Taylor parameter D_{13}^{∞} in Figure 7a. However, as the NH law is

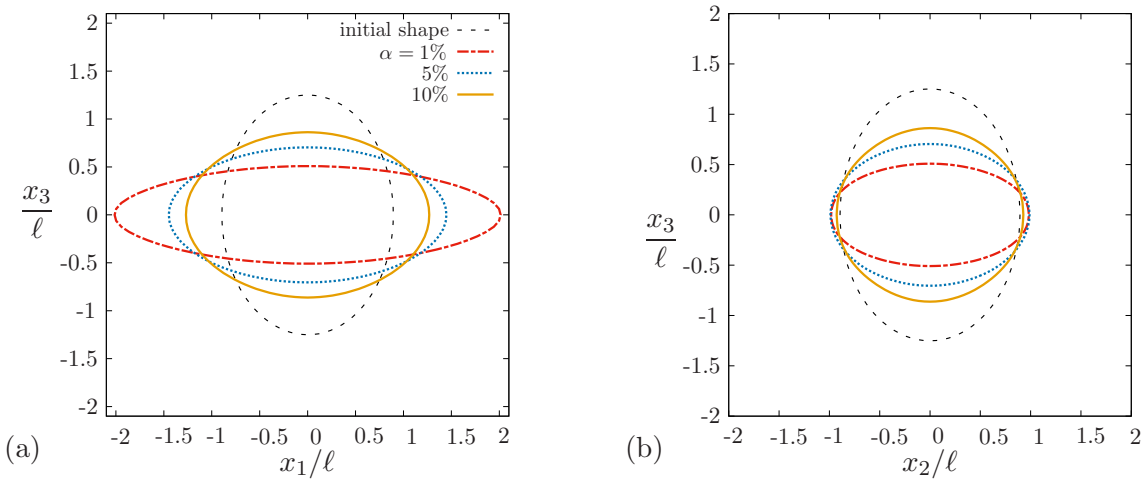

Figure 9: Influence of α on the capsule mid–surface at steady-state ($Ca_v = 0.015$, GH law). Mid–surface cross profiles in the flow plane (a) and in the perpendicular plane (b).

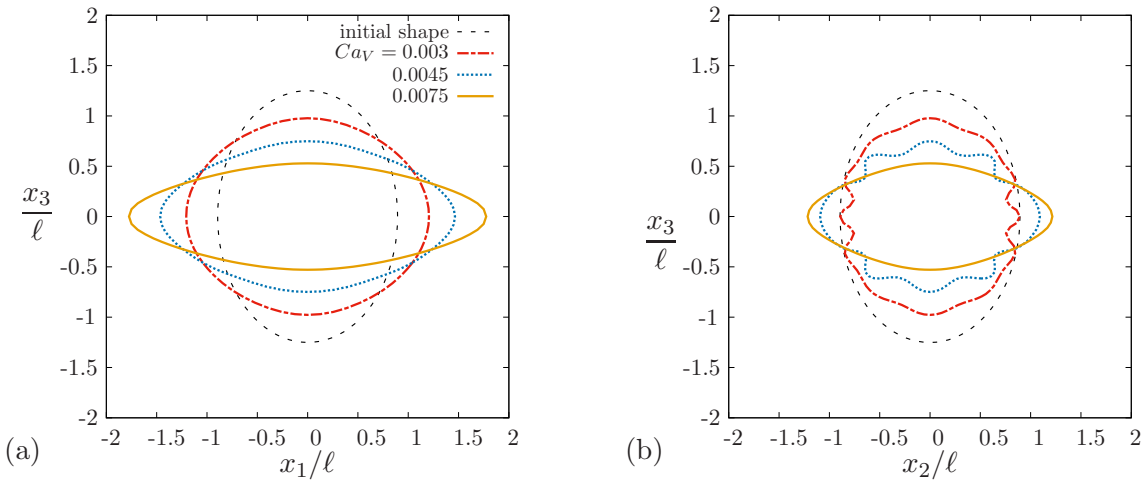

Figure 10: Influence of Ca_v on the capsule mid–surface deformation at steady-state ($\dot{\gamma}t = 5$, $\alpha = 3\%$, NH law). Mid–surface cross profiles in the flow plane (a) and in the perpendicular plane (b).

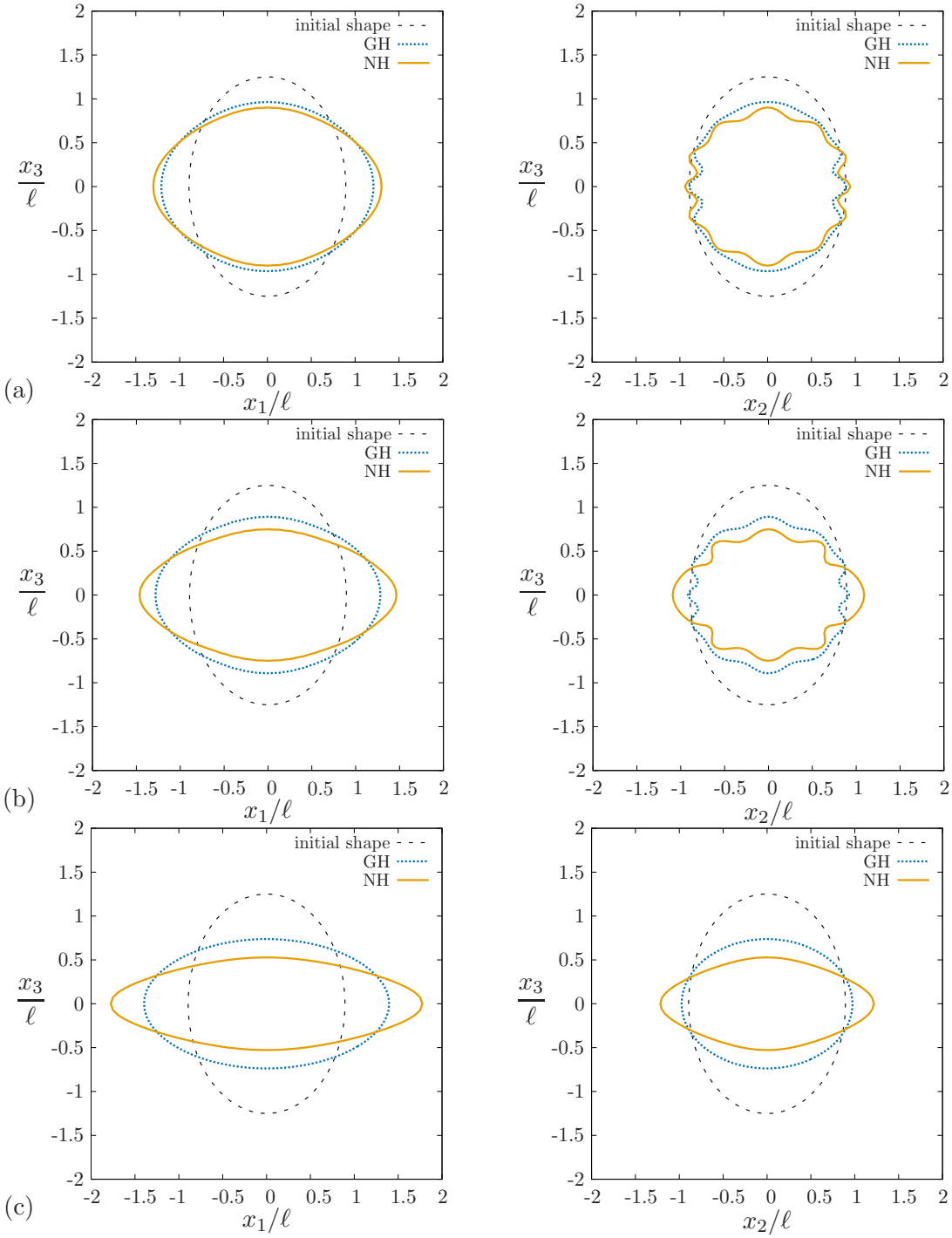

Figure 11: Influence of the constitutive law on the capsule mid–surface deformation at steady-state ($\alpha = 3\%$) at $Ca_v = 0.0003$ (a), 0.0045 (b), 0.0075 (c). Mid–surface cross profiles in the flow plane are represented in left and in the perpendicular plane in right.

strain-softening, for a given Ca_v, the capsule is more stretched in the flow direction than with the strain-hardening generalized Hooke's law. It follows that the values of D_{13}^{∞} are larger for a NH wall than for a GH wall. For $0.003 \leq Ca_v \leq 0.006$, the maximum bending to membrane energy ratio $max(E_b(N_i)/E_m(N_i)$ is larger than 20%. Wrinkles appear in the central region (Figure 10b), with a fairly large amplitude. The mid–surface constitutive law thus influences also the wrinkle formation in the central region.

Figure 11 compares the capsule deformed profiles obtained with two different membrane laws, for the case $\alpha = 3\%$ and for the three values of capillary number of Figure 10 with the objective to better visualize the influence of the mid–surface constitutive law. We clearly see that the capsule is more elongated in the flow plane (x_1x_3) for the strain-softening NH law than for the strain-hardening GH law. But the most interesting aspect is the large difference in post-buckling shapes observed within the perpendicular plane (x_1x_2). Both the wrinkle wavelength and amplitude are smaller for the GH law than for the NH law. This indicates that buckled shapes strongly depend on the capsule wall mechanical behaviour.

5.5. Comparison with a membrane model

We now compare the results obtained with either the GSMB model or a classical membrane model, as described in Section 2.3.3. We use the NH law and consider a thickness ratio $\alpha = 3\%$ for the shell model. The relevant parameter for the comparison is the surface capillary number Ca_s, defined in Eq. (37). We take $Ca_s = 0.15$, for which buckling occurs. The GSMB results thus correspond to $Ca_v = 0.0045, \alpha = 3\%, Ca_s = 0.15$. Two different mesh types with 5120 or 8192 elements are also used for the comparison. The deformed mid–surface profiles are shown in Figure 12. In the flow plane (x_1x_3), the profiles obtained with a 5120–element mesh, for either a membrane or 3%-thickness GSMB model coincide very well (Figure 12a). The same remark applies for higher values of thickness up to $\alpha = 10\%$ and for the 8192–element mesh (not shown). However, such is not the case in the cross plane, where buckling occurs. The buckled shape predicted by the GSMB model is stable and does not depend on the type of mesh (Figure 12b), as was mentioned in section 4.2. However, for the membrane model, which is devoid of bending resistance, buckling is only controlled by numerical parameters, such as the mesh size and/or structure. When part of the wall is undergoing compression, the deformed profile depends on the surface grid, as indicated clearly in Figure 12c. It follows that the buckled profile predicted by the membrane model is unphysical and

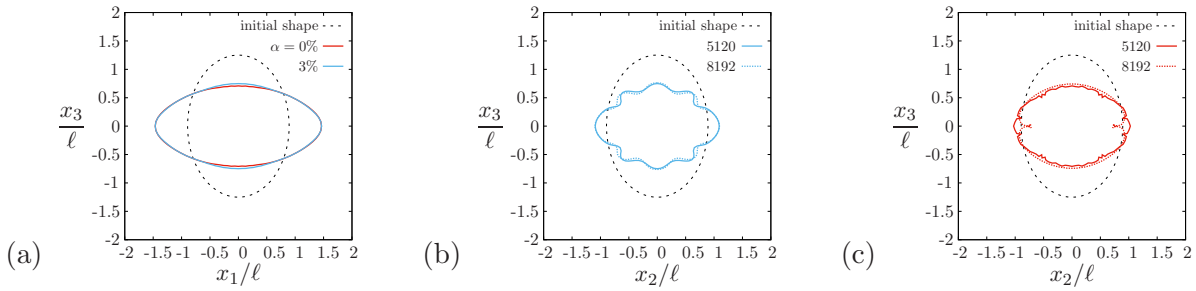

Figure 12: Mid–surface profiles at steady-state (NH membrane) obtained with a membrane model ($Ca_s = 0.15$) or with a GSMB model ($Ca_v = 0.0045, \alpha = 3\%, Ca_s = 0.15$) and two meshes types (5120 or 8192 elements). (a) Membrane and GSMB profiles in the flow plane: the profiles obtained with 5120 elements are almost superimposed; (b) GSMB profiles in the cross-plane: the profiles are independent of the mesh type; (c) membrane model profiles in the cross-plane: the profiles strongly depend on the mesh type.

	L_1	L_2	L_3	Le_1	Le_2	Le_3
membrane	1.46	1.03	0.71	1.46	1.00	0.67
$\alpha = 3\%$	1.46	1.09	0.75	1.45	1.03	0.67
$\alpha = 10\%$	1.45	1.13	0.77	1.41	1.04	0.70

Table 1: Geometrical characteristics of the deformed profile obtained with a membrane or shell model for $Ca_s = 0.15$: L_i and Le_i are the axial lengths of the actual profile or of the ellipsoid of inertia, respectively.

differs significantly from the one obtained when bending resistance is properly taken into account.

For high flow strength, e.g. $Ca_s = 0.25$, the wall is stretched enough that no buckling occurs. In this situation, the membrane and shell models predict the same deformed profile, typically like the ones shown in Figure 11c for $Ca_v = 0.0075$ and $\alpha = 3\%$.

It is customary to compute the capsule deformation by replacing the actual deformed lengths L_i with the three principal axes Le_i of the mid-surface ellipsoid of inertia. This procedure tends to smooth out oscillations of the profile and thus alleviates any error on the details of the buckled surface. When comparing the deformation values obtained with the shell or membrane models (Table 1) we find that the difference in the actual lengths L_i between the membrane and shell models is at most 10%. This difference decreases to $3-4\%$ when we use the lengths of the ellipsoid of inertia, Le_i.

6. Discussion and conclusion

When a capsule is suspended in a flowing liquid, there are situations where part of the capsule wall is subjected to compressive stresses and thus tends to buckle. In order to account for such a phenomenon, the dynamics of the solid wall must include bending effects. We have thus designed the GSMB thin shell model, which takes into account the shear deformation across the capsule wall thickness. Compared to more elaborate shell models like thick- or 3D-shell models [31], the advantage of the GSMB model is that it allows accounting for wall materials that have nonlinear material properties and are either strain-hardening or softening under extension. However, the deformation and stresses in the wall thickness are simplified to leading order with a linear constitutive law. This simplification is made possible by the thinness assumption, whereby terms $O(\alpha^2)$ and higher are neglected compared to terms $O(\alpha)$. The advantage of the model is that it is numerically well behaved and does not lead to numerical locking artefacts [22]. The computational cost of the GSMB model is about 40% higher than that of a simple membrane model, when used in a typical capsule flow problem.

The question that arises is then: when should we use a GSMB to model the capsule wall? In the case of a spherical capsule with a GH membrane, subjected to unbounded shear flow, Dupont et al. [18, 19] show that for high shear rates and any thickness, the predictions of a basic shell shell model are the same as those of the well documented membrane model. This is due to the fact that a spherical capsule must extend its wall surface area in order to deform at constant volume: stretching of the mid–surface is then the dominant phenomenon. In this situation, bending effects are only important at low shear rates where buckling occurs. A GSMB (or a simple SMB model) must be used to predict the fold characteristics (wavelength, amplitude) as a function of α and Ca. Note that, since folds occur at low shear rate (i.e. low deformation), the specific constitutive law of the membrane is irrelevant, so that a basic shell model model can be used.

However, when the initial reference shape of the capsule is not spherical, part of the membrane can be subjected to compressive stresses even at large deformation. This phenomenon occurs for an ellipsoidal capsule freely suspended in shear flow. As an illustration we have chosen the simple case of an ellipsoidal capsule subjected to plane hyperbolic flow: the advantage of this configuration is that the capsule does not rotate and only deforms. We then show that, for stringent deformations, the profiles obtained with a membrane model are significantly different from those

obtained when bending resistance is accounted for. The difference appears in the cross flow plane, where the membrane buckles. We also show that the buckling behavior depends on the membrane constitutive law. It is interesting to note that this phenomenon may stay hidden both numerically or experimentally if only the profile in the flow plane is analyzed.

There are other more complex situations where we can expect bending resistance to alter the motion and deformation of a capsule. The case of an ellipsoidal capsule in simple shear flow is one of them. Another situation is confined flow, where even a spherical capsule is undergoing curvature inversion with associated bending effects.

The GSMB model is developed for thin walled capsules. It will be interesting in the future to study its domain of validity. It is likely that the GSMB model will remain valid even for thick wall capsules under unconfined flows, similarly to what was shown for cylindrical tubes [32]. If thicker walled capsules need to be considered under confined flows, the thin shell model is no longer appropriate: the wall must be treated as a three-dimensional medium with distinct outer and inner boundaries. We then loose the thin shell advantage; i.e. that all quantities, solid and fluid, are evaluated on the mid-surface and that the same grid is used for the fluid and solid problems.

The GSMB model is developed for thin walled capsules with a thickness ratio less or equal typically to $\sim 10\%$. If thicker walled capsules need to be considered, the wall must be treated as a three-dimensional medium with distinct outer and inner boundaries. We then loose the thin shell advantage, i.e. that all quantities, solid and fluid, are evaluated on the mid-surface and that the same grid is used for the fluid and solid problems. Altogether, a comparison between results obtained with either the thin shell model or a three-dimensional wall, should establish the range of validity of the GSMB model, which may depend on the flow configuration.

Acknowledgements

This work received funding from the European Research Council (ERC) under the European Unions Horizon 2020 research and innovation programme (Grant agreement No. ERC-2017-COG - MultiphysMicroCaps).

References

[1] K. S. Chang, W. L. Olbricht, Experimental studies of the deformation and breakup of a synthetic capsule in steady and unsteady simple shear flow, J. Fluid Mech. 250 (1993) 609 –

633.

[2] A. Walter, H. Rehage, H. Leonhard, Shear–induced deformation of polyamid microcapsules, Colloid Polymer Sci. 278 (2000) 169 – 175.

[3] I. Koleva, H. Rehage, Deformation and orientation dynamics of polysiloxane microcapsules in linear shear flow., Soft Matter 8 (2012) 3681 – 3693.

[4] T. X. Chu, A.-V. Salsac, E. Leclerc, D. Barthès-Biesel, H. Wurtz, F. Edwards-Lévy, Comparison between measurements of elasticity and free amino group content of ovalbumin microcapsule membranes: Discrimination of the cross–linking degree, J. Colloid Interf. Sci. 355 (1) (2011) 81 – 88.

[5] T. X. Chu, A.-V. Salsac, D. Barthès-Biesel, L. Griscom, F. Edwards-Lévy, E. Leclerc, Fabrication and in-situ characterization of microcapsules in a microfluidic system., Microfluid Nanofluid 14 (2013) 309 – 317.

[6] J. Gubspun, P.-Y. Gires, C. De Loubens, D. Barthès-Biesel, J. Deschamps, M. Georgelin, M. Leonetti, E. Leclerc, F. Edwards-Lévy, A.-V. Salsac, Characterization of the mechanical properties of cross-linked serum albumin microcapsules: effect of size and protein concentration, Colloid Polym Sci 294 (2016) 1381–1389.

[7] J. Walter, A.-V. Salsac, D. Barthès-Biesel, P. Le Tallec, Coupling of finite element and boundary integral methods for a capsule in a Stokes flow, Int. J. Num. Meth. Engng 83 (2010) 829 – 850.

[8] D. Barthès-Biesel, Motion and deformation of elastic capsules and vesicles in flow, Annu. Rev. Fluid Mech. 48 (1) (2016) 25–52.

[9] W. Helfrich, Elastic properties of lipid bilayers: theory and possible experiments, Z. Naturforsch. (C) 28 (11) (1973) 693.

[10] C. Pozrikidis, Effect of membrane bending stiffness on the deformation of capsules in simple shear flow, J. Fluid Mech. 440 (2001) 269 – 291.

[11] D. V. Le, Effect of bending stiffness on the deformation of liquid capsule enclosed by thin shells in shear flow., Phys. Rev. E 82 (2010) 016318.

[12] A. Yazdani, P. Bagchi, Influence of membrane viscosity on capsule dynamics in shear flow, J. Fluid Mech. 718 (2013) 569 – 595.

[13] A. Guckenberger, M. P. Schraml, P. G. Chen, M. Leonetti, S. Gekle, On the bending algorithms for soft objects in flows, Comput. Phys. Commun 207 (2016) 1 – 23.

[14] A. Guckenberger, S. Gekle, Theory and algorithms to compute helfrich bending forces: a review, J. Phys. Condens. Matter 29 (20) (2017) 203001.

[15] F. Edwards-Lévy, M.-C. Andry, M.-C. Lévy, Determination of free amino group content of serum albumin microcapsules: II. effect of variations in reaction time and in terephthaloyl chloride concentration, Int. J. Pharm. 103 (3) (1994) 253 – 257.

[16] Z. Y. Xiang, Y. C. Lu, Y. Zou, X. C. Gong, G. S. Luo, Preparation of microcapsules containing ionic liquids with a new solvent extraction system., React. Funct. Polym. 68 (8) (2008) 1260 – 1265.

[17] D. V. Le, Z. Tan, Large deformation of liquid capsules enclosed by thin shells immersed in the fluid., J. Comput. Phys. 229 (2010) 4097 – 4116.

[18] C. Dupont, A.-V. Salsac, D. Barthès-Biesel, M. Vidrascu, P. Le Tallec, Influence of bending resistance on the dynamics of a spherical capsule in shear flow, Phys. Fluids 27 (5) (2015) 051902.

[19] C. Dupont, P. Le Tallec, D. Barthès-Biesel, M. Vidrascu, A.-V. Salsac, Dynamics of a spherical capsule in a planar hyperbolic flow: Influence of bending resistance, Procedia IUTAM 16 (2015) 70 – 79.

[20] X.-Y. Wang, A. Merlo, C. Dupont, A.-V. Salsac, D. Barthès-Biesel, Characterization of the mechanical properties of microcapsules with a reticulated membrane: comparison of microfluidic and microrheometric approaches 1 E8.

[21] A. Walter, H. Rehage, H. Leonhard, Shear induced deformation of microcapsules: shape oscillations and membrane folding, Colloid Surface A 183 – 185 (2001) 123 – 132.

[22] D. Chapelle, K. J. Bathe, The Finite Element Analysis of Shells – Fundamentals (Computational Fluid and Solid Mechanics). Second Edition, Springer, 2011.

[23] C. Dupont, Biomécanique de capsules en écoulement., Ph.D. thesis, Ecole Polytechnique (2014).

[24] D. Barthès-Biesel, A. Diaz, E. Dhenin, Effect of constitutive laws for two dimensional membranes on flow-induced capsule deformation, J. Fluid Mech. 460 (2002) 211 – 222.

[25] D. Chapelle, A. Ferent, K. Bathe, 3D-shell elements and their underlying mathematical model, Mathematical Models and Methods in Applied Sciences 14 (1) (2004) 105–142.

[26] J. Walter, A.-V. Salsac, D. Barthès-Biesel, Ellipsoidal capsules in simple shear flow: prolate versus oblate initial shapes, J. Fluid Mech. 676 (2011) 318 – 347.

[27] P.-S. Lee, K.-J. Bathe, Development of MITC isotropic triangular shell finite elements, Comput. Struct. 82 (11-12) (2004) 945 – 962.

[28] J.-L. Batoz, G. Dhatt, Modélisation des structures par éléments finis: Coques, Hermès, 1992.

[29] M. Bonnet, A. Frangi, C. Rey, The finite element method in solid mechanics, P. Roncoroni, 2014.

[30] E. Foessel, J. Walter, A.-V. Salsac, D. Barthès-Biesel, Influence of internal viscosity on the large deformation and buckling of a spherical capsule in a simple shear flow, J. Fluid Mech. 672 (2011) 477 – 486.

[31] D. Chapelle, A. Férent, K. Bathe, 3D-shell elements and their underlying mathematical model, Math Mod. Meth. Appl. S. 14 (2004) 105–142.

[32] A. J. Sadowski, J. M. Rotter, Solid or shell finite elements to model thick cylindrical tubes and shells under global bending, Int. J. Mech. Sci. 74 (2013) 143–153.